Check for updates

Strategies for imaging with Marchenko-retrieved Green's functions

Satyan Singh[1] and Roel Snieder[1]

ABSTRACT

Recent papers show that imaging with the retrieved Green's function constructed by the Marchenko equations, called Marchenko imaging, reduces artifacts from internal and free-surface multiples compared with standard imaging techniques. Even though artifacts are reduced, they can still be present in the image, depending on the imaging condition used. We have found that when imaging with the up- and downgoing Green's functions, the multidimensional deconvolution (MDD) imaging condition yields better images than correlation and deconvolution. "Better" in this case means improved resolution, fewer artifacts, and a closer match with the true reflection coefficient of the model. We have determined that the MDD imaging condition only uses primaries to construct the image, whereas multiples are implicitly subtracted in the imaging step. Consequently, combining the first arrival of the downgoing Green's function with the complete upgoing Green's function produces superior (or at least equivalent) images than using the one-way Green's functions because the first arrival of the downgoing Green's function excludes all the downgoing multiply reflected waves. We also find that standard imaging algorithms which use the redatumed reflection response, constructed with the one-way Green's functions, produce images with reduced artifacts from multiples compared with standard imaging conditions, which use surface reflection data. All imaging methods that rely on the Marchenko equations require the same inputs as standard imaging techniques: the reflection response at the surface and a smooth estimate of the subsurface velocities.

INTRODUCTION

The Marchenko equations can be used to retrieve the up- and downgoing Green's function between an arbitrary virtual receiver in the subsurface and a source on the surface. However, these equations do not prescribe how to use the Green's function for imaging. The purpose of this paper is to explain and compare different strategies for imaging using these up- and downgoing Green's functions. Imaging using these Green's functions is called Marchenko imaging. Standard imaging techniques assume single scattering, and therefore misposition multiple-reflection events in the image. However, imaging with the Marchenko-retrieved Green's functions significantly reduces (if not eliminates) the artifacts associated with multiple reflections (Slob et al., 2014; Wapenaar et al., 2014; Singh et al., 2015, 2016). There are many types of imaging conditions that can be used to image the subsurface with the Marchenko Green's functions; they are, however, mostly restricted to imaging with Green's functions that include only primaries and internal multiples, and they have never been systematically compared for imaging artifacts.

Broggini et al. (2011) show that one can retrieve at the surface the up- and downgoing Green's function in 1D at a point (virtual source) in the subsurface. These Green's functions include primaries and internal multiples. Wapenaar et al. (2012) extend the Green's function retrieval to 3D by posing the problem as a multidimensional Marchenko equation, which is then solved iteratively. Imaging using the Marchenko-retrieved Green's functions is first proposed in 1D by Wapenaar et al. (2011), using deconvolution of the associated up- and downgoing Green's functions at zero lag. Behura et al. (2012) apply the Marchenko Green's functions to image specific target locations in the 2D synthetic model, using a correlation imaging condition. This imaging condition is defined as the correlation of the up- and downgoing Green's function at each image point in the subsurface at zero lag and zero offset.

Broggini et al. (2014) show that the image constructed by multidimensional deconvolution (MDD) (Wapenaar et al., 2008; van der Neut et al., 2011) of the up- and downgoing Green's function produces a similar image of the subsurface, compared with the correlation image (Behura et al., 2012); however, the MDD image better

matched the true reflectivity of the model. Imaging with MDD significantly reduces imaging artifacts when compared with standard imaging techniques, such as reverse time migration (RTM) and downward continuation (Broggini et al., 2014; Slob et al., 2014; Wapenaar et al., 2014). These imaging artifacts are due to the presence of internal multiples in the data that are not properly handled.

Singh et al. (2015, 2016) modify the Marchenko equations to not only include primaries and internal multiples but also free-surface multiples. These modified Marchenko equations obviate the need to remove the free-surface multiples from the reflection response before computing the Green's functions. The free surface is the strongest reflector in the earth, and free-surface multiples are generally stronger than internal multiples. Free-surface multiples can even be as strong as primaries (Weglein and Dragoset, 2007). For models with free-surface multiples, Singh et al. (2016) show that the MDD image with Marchenko Green's functions reduces imaging artifacts due to the multiples when compared with RTM.

We investigate different imaging conditions for the Green's functions that include primaries, internal multiples, and free-surface multiples (see Table 1). In addition to the correlation- and deconvolution-imaging conditions using the up- and downgoing Green's functions $G^{\pm}$, we also image the subsurface with the first arrival of the downgoing Green's function G_f^+ and the upgoing Green's function G^-. Bakulin and Calvert (2006) and Mehta et al. (2007) show that muting the wavefield recording at the virtual source location, so that it is limited to its first arrival, improves the virtual source method. This muting suppresses spurious events in the virtual source gather. We use the same concept of muting the first arrival of G^+ to further reduce the imaging artifacts from multiples in the Marchenko image.

For simplicity, we separate our investigation on Marchenko imaging strategies into 1D and 2D. In our 1D investigation, we consider analytical and numerical examples that investigate the strengths and weaknesses of each imaging condition given in Table 1. We also compare each imaging condition using either the up- and downgoing Green's functions or the up- and first arrival of the downgoing Green's functions. The conclusion of our 1D analysis is used to complement our analysis in the 2D scenario. In our 2D investigation, we compare imaging with a standard imaging technique, RTM, and Marchenko imaging.

1D STRATEGIES FOR IMAGING

In this section, we restrict our imaging and theory to 1D. However, the ideas, conclusions, and analyses are applicable, for the most part, to multidimensions. The imaging conditions analyzed in this section are (1) correlation and (2) deconvolution. We also compare the application of these imaging conditions to either the upgoing Green's function G^- and downgoing Green's function G^+ or to the upgoing Green's function G^- and first arrival of the downgoing Green's function G_f^+. In addition, we investigate the retrieval of the redatumed reflection response using correlation and deconvolution. A summary of our findings are shown in Table 1. For completeness and simplicity, we analyze each imaging condition in 1D; in two parts: an analytical investigation and a numerical investigation. Our analytical model is shown in Figure 1, whereas our numerical model is shown in Figure 2.

Note that our analytical and numerical models are different. The numerical model has a free surface at the acquisition surface in contrast to the transparent surface of our analytical model. Omitting the free surface in the analytical model in Figure 1 greatly simplifies the mathematics and interpretation. The details of the Green's function retrieval for our analytical model are given in Appendix A.

For our 1D models, we denote the depth as z_i, where the subscript $i = 0, 1, 2, \ldots$ corresponds to the depth in 1D; for instance, z_0 is the acquisition surface. Superscript $(+)$ refers to downgoing waves and $(-)$ to upgoing waves at the depth z. Any variable with a subscript 0 that is not the coordinate field z (e.g., R_0) indicates that no free surface is present. We start with an overview of the analytical

Table 1. Summary of the imaging conditions we use in this paper. All imaging conditions, be it correlation, deconvolution, or multidimensional deconvolution, are taken at zero time and zero offset to construct the image. The G^+, G^-, and G_f^+ are the downgoing, upgoing, and first arrival of the downgoing Green's function at the image point, respectively. The tick marks (✓) mean that the condition at the top of the column holds, whereas (X) means that the condition is not satisfied.

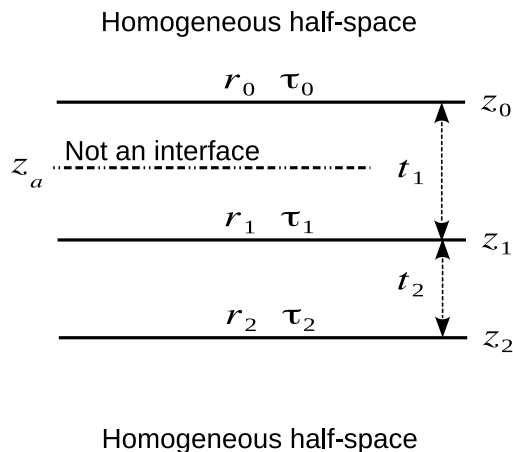|	True reflectivity image		Correct position of interfaces = No False interfaces		Correct Redatum reflection response	
Imaging	G^+ with G^-	G_f^+ with G^-	G^+ with G^-	G_f^+ with G^-	G^+ with G^-	G_f^+ with G^-
Correlation	✗	✗	✗	✓	✗	✗
Deconvolution for 1D image	✓	✓	✓	✓	✓	✗
Deconvolution for 2D image	✗	✗	✗	✓	✗	✗
Multidimensional deconvolution	✓	✓	✓	✓	✓	✗

Figure 1. Analytical 1D model for retrieval of the Green's functions and imaging. The model is used to compute the reflection response for sources and receivers just as the first layer z_0.

and numerical investigations before evaluating each imaging condition in 1D.

Analytical investigation

We use a three-interface (two-layer) model with the first interface just below the acquisition surface. The analytical expression for the reflection response for such a model (see Figure 1; equation A-1) is given by Goupillaud (1961). The analytical model does not include a free surface; however, the ideas for this simple model can be extended to models with a free surface. In Appendix A, we discuss in detail the retrieval of the Green's function for the analytical model in Figure 1.

We retrieve the Green's function at a virtual receiver in the subsurface using equations A-4 and A-5 (Broggini et al., 2012; Broggini and Snieder, 2012; Wapenaar et al., 2013, 2014; Slob et al., 2014; Singh et al., 2015, 2016). In our analytical investigation, we retrieve the Green's functions at two virtual receiver locations: (1) in the middle of the first layer ($z = z_a$) and (2) just above the second interface ($z = z_1$), in Figure 1. The expressions for the up- and downgoing Green's functions $G^{\pm}$ at $z = z_a$ and $z = z_1$ are given by equations A-8, A-9, A-14, and A-13. We chose these locations because there is no interface at z_a, whereas immediately below, at z_1, there is an interface with reflection coefficient r_1, as shown in Figure 1.

Numerical investigation

Unlike the analytical investigation, we use the model in Figure 2, which has variable density and constant velocity, to numerically image the subsurface using the Marchenko retrieved Green's functions. Although here we use a constant velocity model, the Marchenko equations and the corresponding imaging methods are applicable to media with variable velocities. Our analytical work is restricted to imaging at only two locations in Figure 1, whereas our numerical investigation computes the image at 5 m intervals in the numerical model in Figure 2. Each image point corresponds to a virtual receiver location of the Green's function. We compute the up- and downgoing Green's functions at each virtual receiver location in the subsurface for sources on the surface.

We build our intuition of imaging with these Green's functions by analyzing snapshots of these Green's functions (see Figure 3) at all virtual receiver locations. For example, in Figure 3a and 3b, when G^+ reaches the first interface at 1.5 km, it generates an upgoing wave in the Green's function G^-. In Figure 3b, G^+ and G^- are kinematically equivalent at the interface, and we exploit this kinematic equivalence to determine the position and reflection coefficient of the interface.

In addition, a multiple (labeled A) is generated at the free surface in Figure 3e. This multiple can also become kinematically equivalent with other reflections in G^- (labeled B) in Figure 3f, which can cause imaging artifacts (false interfaces) depending on the imaging condition. However, this free-surface multiple in G^+ (labeled A in Figure 3e and 3f) also interacts with the interfaces and creates an associated upgoing wave in G^-.

This intuition of kinematic similarity between waves at interfaces is related to the work of Claerbout (1985), who has shown that the up- and downgoing wavefields at an arbitrary datum can be used for imaging. Hence, we can use the up- and downgoing retrieved Green's function at the virtual receiver location to image the subsur-

face. The governing equation for imaging with up- and downgoing wavefields in 1D is

$$G^-(z_i, z_0, t) = \int_{-\infty}^{\infty} G^+(z_i, z_0, t - t')R_0(z_i, z_i, t')dt', \quad (1)$$

where z_i is an arbitrary depth level and R_0 is the reflection response of the medium below z_i (Claerbout, 1985; Amundsen, 2001; Wapenaar et al., 2008). In this expression, $R_0(z_i, z_i, t)$ is the reflection response for sources and receivers at z_i, with the medium above z_i being homogeneous.

The image of the subsurface is $R_0(z_i, z_i, t = 0)$, the reflection response R_0 at zero time. Intuitively, for a source and a receiver coincident at an interface z_i, the zero-time response $R_0(z_i, z_i, t = 0)$ at that location is the contribution to the image corresponding to the interface. Similarly, in the absence of an interface at z_i, the contribution of $R_0(z_i, z_i, t = 0)$ at the zero time is zero.

We now investigate the Marchenko imaging conditions as summarized in Table 1: (1) correlation and (2) deconvolution. The last column of Table 1, obtaining the correct redatumed reflection response, is investigated as a separate subsection in this 1D imaging strategies segment.

Imaging condition: Correlation

In this section, we introduce the correlation imaging condition to the Marchenko wavefields and discuss the advantages and disadvantages to applying this imaging condition to our analytical model (Figure 1) and our numerical model (Figure 2). Note that, in comparison with the analytical model, the numerical model includes a free surface, but the reader should appreciate the similarities in the imaging results for each model.

The contribution at the zero-lag correlation of two 1D signals is due to kinematically similar events in the signals. For this reason, standard imaging techniques, for example, RTM, generally use the crosscorrelation at zero lag as the contribution to the image (Baysal et al., 1983; Whitmore, 1983; McMechan, 1989). As discussed in the previous section, kinematically similar events in the up- and downgoing Green's function are generally the location of the interfaces. However, unlike the Marchenko wavefields, the fields used in
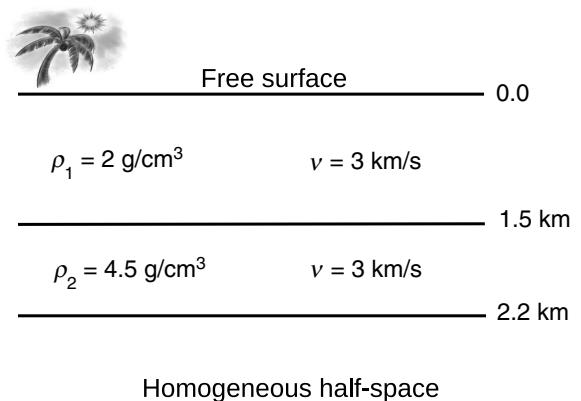

Figure 2. Numerical 1D model with a free surface and constant velocity of 3 km/s. The Green's functions are retrieved at each position in space to create snapshots of the wavefields propagating through this model. We use this model in our 1D strategies for the imaging section to describe our numerical investigation in 1D.

conventional RTM assume the first-order Born approximation, and therefore RTM has artifacts when the data have multiples (O'Brien and Gray, 1996; Glogovsky et al., 2002).

In the time domain, the zero-lag correlation-imaging condition in 1D for the retrieved up- and downgoing Green's function is

$$C(z_i, z_0, t = 0) = \int_{-\infty}^{\infty} G^-(z_i, z_0, t') G^+(z_i, z_0, t') dt'. \quad (2)$$

Equation 2 means that the correlation image is the time integral of the up- and downgoing Green's function.

Analytical investigation

In this subsection of correlation imaging, we investigate mathematically the correlation imaging condition (equation 2) applied to the 1D model in Figure 1. To illustrate the properties of the correlation image at the center of the first layer $z = z_a$ and at the top of the second interface $z = z_1$ for our analytical example in Figure 1, we first perform a series expansion of the respective up- and downgoing Green's function given in equations A-8, A-9, A-13, and A-14. We first analyze the image at the center of the first layer $z = z_a$, where there is no interface.

The series expansion of the upgoing Green's functions G^- (equation A-8) at the center of the first layer is

$$G^-(z_a, z_0, \omega) = \tau_0 \left\{ r_1 e^{-\frac{3}{2}i\omega t_1} + r_2 e^{-i\omega(\frac{3}{2}t_1 + 2t_2)} + \cdots \right\}, \quad (3)$$

where r_1, r_2, t_1, and t_2 are the reflection coefficients and one-way traveltimes of the first and second layers, respectively; τ_0 is the transmission coefficient of the first interface (see Figure 1); and $\ldots$ represents the higher order terms in the reflection coefficients of the series. The series expansion of three follows from the geometric series rule $1/(1 - r) = \sum_{k=0}^{\infty} r^k$. The inverse Fourier transform of equation 3 is

$$G^-(z_a, z_0, t) = \tau_0 \left\{ r_1 \delta\left(t - \frac{3}{2}t_1\right) + r_2 \delta\left(t - \frac{3}{2}t_1 - 2t_2\right) \right.$$
$$\left. + \cdots \right\}. \quad (4)$$

Additional terms in the series are given in equation A-10, and we verify these terms in Figure 20.

For the downgoing Green's function G^+, the series expansion yields

$$G^+(z_a, z_0, \omega) = \tau_0 \left\{ e^{-\frac{1}{2}i\omega t_1} + r_1 r_2 e^{-i\omega(\frac{5}{2}t_1 + 2t_2)} \right.$$
$$\left. - r_0 r_1 e^{-\frac{5}{2}i\omega t_1} + \cdots \right\}. \quad (5)$$

In the time domain, equation 5 becomes

$$G^+(z_a, z_0, \omega) = \tau_0 \left\{ \delta\left(t - \frac{1}{2}t_1\right) + r_1 r_2 \delta\left(t - \frac{5}{2}t_1 - 2t_2\right) \right.$$
$$\left. - r_0 r_1 \delta\left(t - \frac{5}{2}t_1\right) + \cdots \right\}. \quad (6)$$
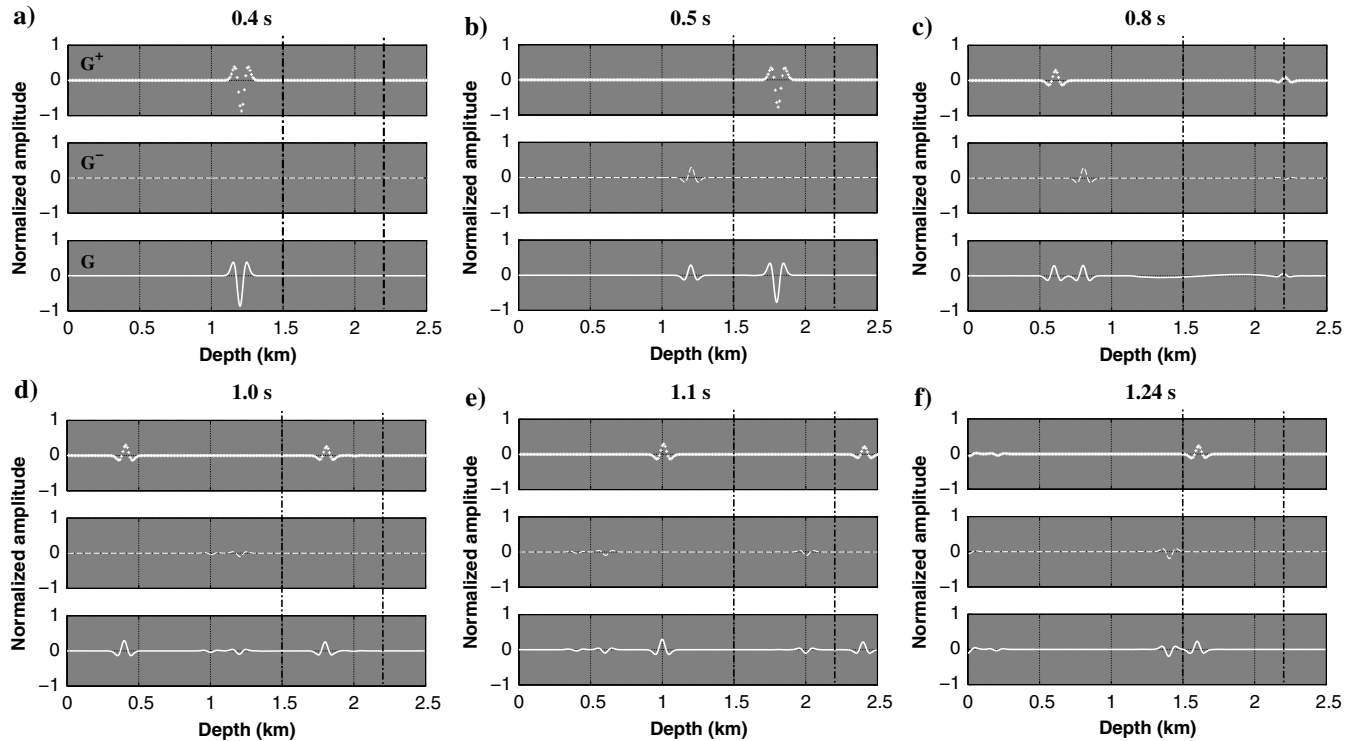

Figure 3. Snapshots of the Green's functions: downgoing $G^+(z, z_0, t)$ (top), upgoing $G^-(z, z_0, t)$ (middle), and total $G(z, z_0, t)$ (bottom) for each figure panel with virtual receivers ranging from 0 to 2.5 km depth. We start at 0.4 s for the model given in Figure 2. The vertical black lines at 1.5 and 2.2 km are the interfaces.

For a model where $t_2 = t_1/2$, the second and third terms of the series in equations 4 and 6, respectively, coincide in time, as shown in Figure 4. From equation 2, the correlation image at $z = z_a$ is $r_0 r_1 r_2 + \cdots$; hence, there is a contribution, although there is no interface at this depth. This contribution to the image at $z = z_a$ is an artifact (false interface) (see Table 1) from an internal multiple in the first layer and a reflection from the second layer, as shown in Figure 4.

At $z = z_1$, the location of the interface, the series expansion of the up- and downgoing Green's functions $G^{\pm}$ in equations A-13 and A-14 yields (in the time domain)

$$G^-(z_1, z_0, t) = \tau_0 \{ r_1 \delta(t - t_1) + r_2 \delta(t - t_1 - 2t_2) + \cdots \},$$
$$G^+(z_1, z_0, t) = \tau_0 \{ \delta(t - t_1) + r_1 r_2 \delta(t - t_1 - 2t_2) + \cdots \}. \quad (7)$$

In equation 7, the events in the up- and downgoing Green's functions occur at the same time; hence, they contribute to the image. The higher order terms in the series expansion of equations A-13 and A-14 also have similar times in the up- and downgoing Green's functions and also contribute to the image at z_1. Therefore, at the interface, all events in the up- and downgoing Green's functions are kinematically equivalent. These events (kinematically the same) are multiplied by each other and integrated in time (equation 2) to produce the correlation image. The contribution to the correlation image at z_1 for the terms in equation 7 is $\tau_0^2 (r_1 + r_1 r_2^2 + \cdots)$ instead of the true amplitude r_1. This is expected as we do not solve equation 1 exactly for R_0 (as shown in Table 1: **x** at the true reflectivity image for correlation imaging).

Numerical investigation

We apply the correlation imaging condition at each virtual receiver location for the associated G^+ and G^-; the corresponding image is shown in Figure 5.

For the actual model in Figure 2, the reflection coefficient of the first layer at 1.5 km is 0.33, whereas the second interface at 2.2 km is 0.38. Comparing the parameters for the actual model with the correlation image in Figure 5 shows that (1) the reflection coeffi-
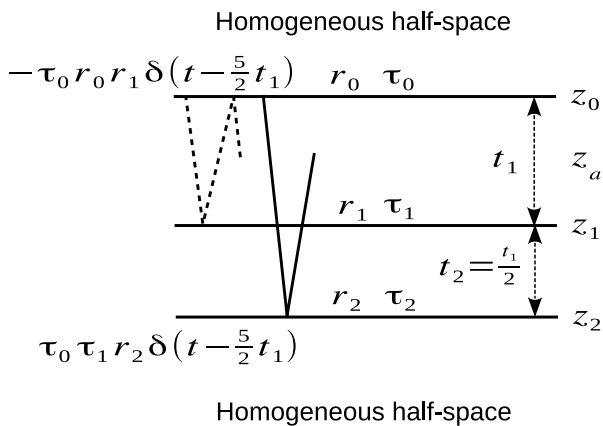
cients of the actual model do not match the correlation image; however, the two interfaces are correctly positioned at 1.5 and 2.2 km, respectively; (2) we obtain a spurious event at 0.7 km in the correlation image that does not match the interfaces in the actual model (refer to Table 1 in the correlation imaging row); and (3) the relative amplitudes of the interfaces in the correlation image are also incorrect.

The presence of the false interface is explained in Figure 3f, where a free-surface multiple in G^+ (labeled A) interacts with the upgoing reflection (labeled B) from the second layer in G^- at approximately 0.7 km. At this depth of 0.7 km, G^+ and G^- have kinematically similar events (waves A and B) and hence an incorrect contribution to the correlation image. This false event at 0.7 km is due to free-surface multiples in G^+ correlating at zero lag with the second layer primary event and also other multiples at later times.

Imaging condition: Deconvolution

In this section, we introduce and apply the deconvolution imaging condition to our analytical and numerical imaging examples. The findings of this subsection are summarized in Table 1. As opposed to the correlation imaging condition, the deconvolution imaging condition is the more mathematically correct way to image the subsurface in 1D (determine the location of reflectors and its parameters).

In the frequency domain, the reflection response R_0 (equation 1) in 1D is a deconvolution

$$R_0(z_i, z_i, \omega) = \frac{G^-(z_i, z_0, \omega)}{G^+(z_i, z_0, \omega)} \Rightarrow \frac{G^-(z, \omega) G^+(z, \omega)^*}{|G^+(z, \omega)|^2 + \epsilon}, \quad (8)$$

where * represents the complex conjugate and ϵ is a regularization parameter to avoid division by zero (Clayton and Wiggins, 1976). The deconvolution imaging condition similar to the correlation imaging condition is R_0 at zero time at the location of the Green's function virtual receiver z_i.

Figure 4. Schematic of a event in the up- and downgoing Green's function at z_a for the one-way traveltime $t_2 = t_1/2$. The reflected wave shown by the solid line represents the second term in equation 3, whereas the dotted line is the third term in equation 5. These events occur at the same time at z_a in their corresponding Green's function; hence, they contribute to the correlation image.
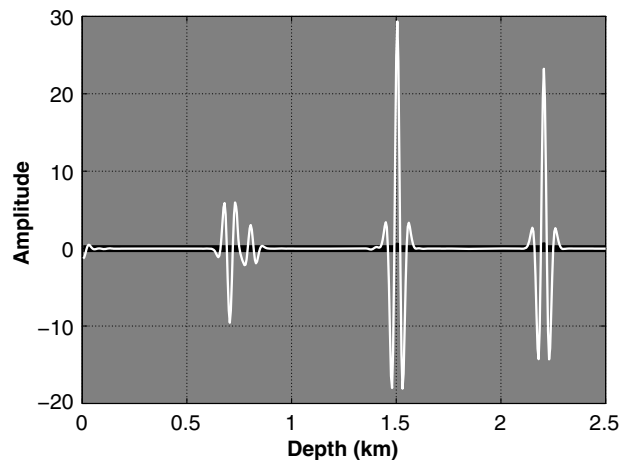

Figure 5. Correlation imaging condition constructed from the up- and downgoing retrieved Green's functions between virtual sources in the subsurface to the surface. We construct these Green's functions at virtual source positions every 5 m in the subsurface.

Analytical investigation

Because we obtain the up- and downgoing Green's function at a point in the subsurface analytically (no noise), solving equation 8 is simply a division of these functions in the frequency domain. We first analyze R_0 at the center of the first layer z_a for the model given in Figure 1. The division of the upgoing by the downgoing Green's function at z_a, given in equations A-8 and A-9, respectively, yields

$$
\begin{aligned}
R_0(z_a, z_a, \omega) &= \frac{G^-(z_a, z_0, \omega)}{G^+(z_a, z_0, \omega)}, \\
&= \frac{r_1 e^{-\frac{3}{2}i\omega t_1} + r_2 e^{-i\omega\left(\frac{3}{2}t_1 + 2t_2\right)}}{e^{-\frac{1}{2}i\omega t_1} + r_1 r_2 e^{-i\omega\left(\frac{1}{2}t_1 + 2t_2\right)}}, \\
&= \frac{r_1 e^{-i\omega t_1} + r_2 e^{-i\omega(t_1 + 2t_2)}}{1 + r_1 r_2 e^{-2i\omega t_2}}, \\
&= \left\{ r_1 e^{-i\omega t_1} + r_2 e^{-i\omega(t_1 + 2t_2)} \right\} \\
&\quad \times \left\{ 1 + \sum_{n=1}^{\infty} (-r_1 r_2 e^{-2i\omega t_2})^n \right\}.
\end{aligned}
\tag{9}
$$

Note that the denominators in G^+ and G^- in equations A-8 and A-9, respectively, cancel by the spectral division in equation 9. The denominators of these Green's functions are the multiple scattered contributions in the Green's function after a series expansion.

The time-domain expression for the series expansion of equation 9 is

$$
R_0(z_a, t) = r_1 \delta(t - t_1) + E(t > t_1),
\tag{10}
$$

where $E(t > t_1)$ are the events in R_0 that occur for $t > t_1$. Equation 10 tells us that the contribution to the image after applying the deconvolution imaging condition $R_0(z_a, t = 0)$ is zero at z_a because there are no contributions at zero time. This vanishing contribution to the image is expected because we do not have any interface at z_a.
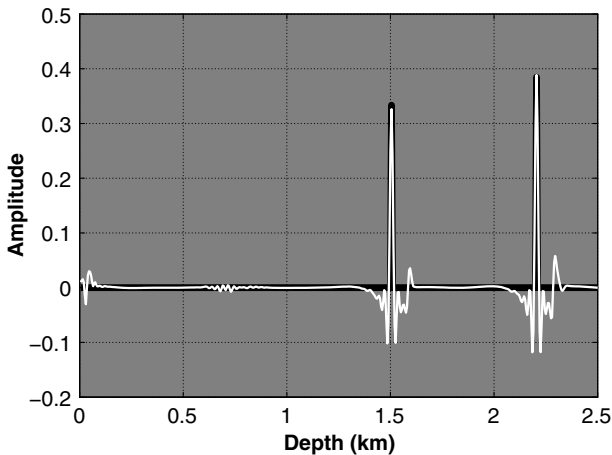

Figure 6. Deconvolution imaging condition constructed from the same up- and downgoing retrieved Green's functions used in the correlation imaging section. The black line represents the exact reflection coefficient of the model in Figure 2.

We now consider R_0 at the second interface z_1 in Figure 1. The reflection response R_0 given by the division of equations A-13 and A-14 yields

$$
R_0(z_1, z_1, \omega) = \frac{G^-(z_1, z_0, \omega)}{G^+(z_1, z_0, \omega)}, \quad = \frac{r_1 + r_2 e^{-2i\omega t_2}}{1 + r_1 r_2 e^{-2i\omega t_2}}.
\tag{11}
$$

Similarly, the time-domain expression for the series expansion of equation 11 is

$$
R_0(z_1, z_1, t) = r_1 \delta(t) + E(t > 0),
\tag{12}
$$

where $E(t > 0)$ are the events in R_0 that occur for $t > 0$. Therefore, considering equation 12, the contribution to the deconvolution imaging $R_0(z_1, z_1, t = 0)$ at the second interface z_1 is r_1. This imaging condition result $R_0(z_1, z_1, t = 0) = r_1$ corresponds to the actual reflection coefficient at the second interface r_1.

Note that the multiple reflections that are embedded in the denominator of equations A-13 and A-14 are removed by the spectral division of G^- and G^+ (equation 11) to produce the image, whereas at zero time only, the first term in the expansion contributes to the image. This is in agreement with the conclusions of Snieder (1990a, 1990b) that the multiples are removed in the inversion to produce the image, whereas only the first Born approximation term, i.e., the primary reflections, contribute to the image. We emphasize that for R_0 at the interface and at zero time, the primary reflections alone contribute to the construction of the image.

Numerical investigation

Using equation 8, we apply the deconvolution-imaging condition to the up- and downgoing Green's function for the numerical model given in Figure 2. The corresponding image is shown in Figure 6 and matches the true reflectivity of the actual model (the solid black line).

Figure 6 conforms well to the conclusions we have made in the analytical work of this section: (1) There are no artifacts in Figure 6 due to kinematically similar events in the up- and downgoing Green's function at 0.7 km compared with the correlation image in Figure 5 and (2) the deconvolution image obtains the correct reflection coefficients at the two interfaces of the model (Figure 2) because we exactly solve for R_0 in 1D. There is a weak artifact in the deconvolution image at 0.7 km; however, these relatively negligible events, compared with the events at the interface, are due to deconvolution numerical error and the finite-recording time of the reflection response at the surface. Therefore, in Table 1, there are tick marks (✓) under the true reflectivity imaging and no false interfaces for deconvolution imaging in 1D, which is corroborated by the analytical and numerical investigations.

Imaging condition: Marchenko redatuming

Once we have a reflection response with the complicated overburden waves removed, we can apply standard imaging algorithms, such as RTM, on this response to image the subsurface. The resulting image, below the overburden, will also be void of any of the overburden artifacts; for instance, the free-surface multiple artifacts will be removed. This section discusses how to obtain a reflection response with the complicated overburden removed and how we can use this response for imaging.

We obtain the reflection response in 1D below an arbitrary point in the model by also solving equation 1 for R_0, as previously stated. We call this reflection response the redatumed reflection response $R_0(z_i, z_i, t)$ because we can interpret $R_0(z_i, z_i, t)$, at depth z_i, as the reflection response for a source at z_i and for receivers at z_i, whereas above z_i the medium is homogeneous. Because the redatumed response $R_0(z_i, z_i, t)$ contains the reflection events below the arbitrary chosen datum, we can use this response to image below an arbitrary datum z_i, thus ignoring the overburden reflection. The function R_0 includes internal multiples from reflections below z_i; therefore, RTM imaging with R_0 will still have artifacts due to the presence of internal multiples generated below z_i.

Analytical investigation

The redatumed response is obtained by solving equation 1. In our 1D analytical model, we solve for R_0 using deconvolution (equation 8). At z_a (the center of the first layer), equation 10, including some higher order terms, gives the redatumed response $R_0(z_a, z_a, t)$ at depth z_a:

$$\begin{aligned}
R_0(z_a, z_a, t) = & \ r_1\delta(t - t_1) + r_2\delta(t - t_1 - 2t_2) \\
& - r_1^2 r_2\delta(t - t_1 - 2t_2) - r_1 r_2^2\delta(t - t_1 - 4t_2) \\
& + r_1^3 r_2^2\delta(t - t_1 - 4t_2) + E(t > t_1 - 4t_2), \\
= & \ r_1\delta(t - t_1) + \tau_1^2 r_2\delta(t - t_1 - 2t_2) \\
& + \tau_1^2 r_1 r_2^2\delta(t - t_1 - 4t_2) + E(t > t_1 - 4t_2).
\end{aligned} \tag{13}$$

In the last line of equation 13, the first three events on the right side are verified in the schematic in Figure 7; notice that we account for transmission through the interfaces.

The $R_0(z_a, z_a, t)$ (equation 13) not only includes the primary events but also the internal multiples, and these reflection events have the correct amplitudes (see Figure 7). Therefore, we can use this redatumed reflection response $R_0(z_a, z_a, t)$ for imaging, which ignores the reflections from above z_a.

Numerical investigation

For our numerical model in Figure 2, we compute the redatumed reflection response at $z = 1.75$ km in Figure 8. This response is the
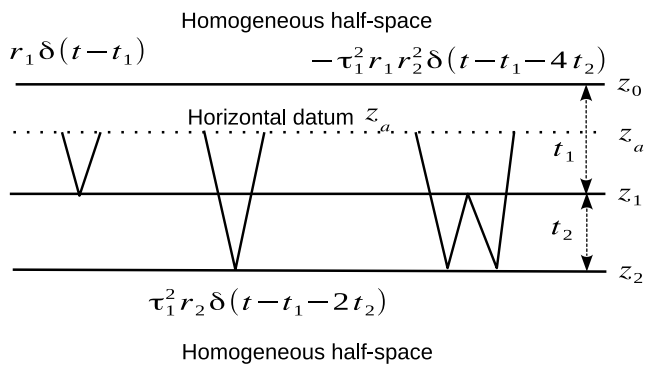
deconvolution of the up- and downgoing Green's functions at the virtual receiver and source at $z = 1.75$ km, below the first layer in Figure 2, i.e., $R_0(z, z, t)$. Below the virtual source at $z = 1.75$ km, our model has one interface at $z = 2.2$ km with a reflection coefficient of 0.38, which is retrieved in the redatumed response in Figure 8 at 0.35 s. We can now use R_0 to image the interface at 2.2 km from above, i.e., at 1.75 km, using any imaging technique that uses reflection recordings to construct an image of the subsurface.

Therefore, we obtain the redatumed reflection response (with the correct amplitudes and kinematics of events) below an arbitrary datum by using deconvolution but not correlation (see Table 1).

Imaging condition: First arrival of G^+ with G^-

In this subsection, we propose using the first arrival of G^+ (defined as G_f^+) and G^- for imaging the subsurface. We begin our analysis with Figure 3 to analyze the snapshots of the Green's function. Up to 0.8 s (Figure 3b and 3c), the first arrival of G^+ (G_f^+) interacts with the two interfaces to generate upgoing reflections, i.e., G^- (G_f^+ and G^- are kinematically similar at the interface). Therefore, when G_f^+ reaches the interface, we get a contribution to the image. We can use the correlation imaging condition and the deconvolution imaging condition for imaging the subsurface with G_f^+ and G^-.

Analytical investigation

For the analytical model given in Figure 1, at z_a (the center of the first layer), the first arrival of G^+ is $G_f^+ = \tau_0\delta(t - [1/2]t_1)$. Because there are no events with similar times in $G_f^+(z_a, z_0, t)$ and $G^-(z_a, z_0, t)$ in equation 4, the contribution to the correlation image at z_a is zero. The other events in G^+, apart from the first arrivals, are the internal multiples or free-surface multiples. In the correlation imaging section, these multiples in G^+ contribute to false interfaces in the image (e.g., at 0.7 km in Figure 4).

The deconvolution of $G^-(z_a, z_0, t)$ (equation A-8) with $G_f^+(z_a, z_0, t)$ in the frequency domain yields

Figure 7. Schematic of a few events in the redatumed reflection response (equation 13) at z_a for the model in Figure 1.
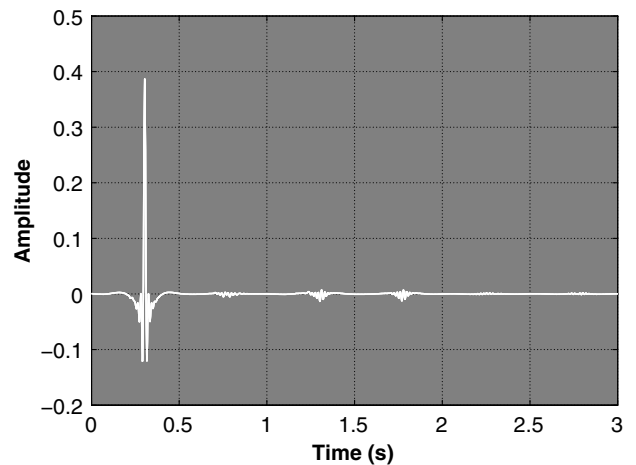

Figure 8. Redatumed reflection response at 1.75 km for the model in Figure 2. Note that below 1.75 km is one interface with a reflection coefficient of 0.38, matching the obtained result.

$$\widetilde{R_0}(z_a, z_a, \omega) = \frac{G^-(z_a, z_0, \omega)}{G_f^+(z_a, z_0, \omega)}$$

$$= \frac{\tau_0 \frac{r_1 e^{-\frac{3}{2}i\omega t_1} + r_2 e^{-i\omega\left(\frac{3}{2}t_1 + 2t_2\right)}}{1 + r_0 r_1 e^{-2i\omega t_1} + r_0 r_2 e^{-2i\omega(t_1 + t_2)} + r_1 r_2 e^{-2i\omega t_2}}}{\tau_0 e^{-\frac{1}{2}i\omega t_1}},$$

$$= \frac{r_1 e^{-i\omega t_1} + r_2 e^{-i\omega(t_1 + 2t_2)}}{1 + r_0 r_1 e^{-2i\omega t_1} + r_0 r_2 e^{-2i\omega(t_1 + t_2)} + r_1 r_2 e^{-2i\omega t_2}}, \tag{14}$$

where $\widetilde{R_0}(z_a, z_a, \omega)$ is not equal to $R_0(z_a, z_a, \omega)$ (equation 9); we are not solving equation 8 because we limit the downgoing Green's function to its first arrival. The time-domain series expansion of equation 14 is

$$\widetilde{R_0}(z_a, z_a, t) = r_1 \delta(t - t_1) + r_2 \delta(t - t_1 - 2t_2)$$
$$+ -r_0 r_1^2 \delta(t - 3t_1) - r_0 r_1 r_2 \delta(t - 3t_1 - 2t_2)$$
$$- r_0 r_1 r_2 \delta(t - 3t_1 - 2t_2) + \cdots . \tag{15}$$

The deconvolution imaging of $\widetilde{R_0}(z_a, z_a, t = 0)$ (equation 15) is zero because there are no terms at the zero time, which agrees with the analytical model (no interface). The $\widetilde{R_0}(z_a, z_a, t)$, for nonzero times, includes spurious events when compared with the correct redatumed response R_0 given in equation 13. Consequently, standard imaging with $\widetilde{R_0}$ as the reflection response would include these spurious events as false interfaces.

At z_1, the first arrival of $G^+(z_1, z_0, t) = G_f^+(z_1, z_0, t) = \tau_0 \delta(t - t_1)$. The correlation image of the analytical model with $G_f^+(z_1, z_0, t)$ and with $G^-(z_1, z_0, t)$ has a contribution at z_1. This contribution is due to the fact that the first term in $G^-(z_1, z_0, t)$ (equation 7) is at the same time as $G_f^+(z_1, z_0, t)$ (kinematically similar events correspond to a contribution to the correlation image). The amplitude of this contribution is $\tau_0^2 r_1$, which differs from the true reflectivity at $z_1 = r_1$ (see Table 1).

Similarly, we can apply deconvolution (equation 8) to $G_f^+(z_1, t)$ and $G^-(z_1, t)$, in the frequency domain; this reads

$$\widetilde{R_0}(z_1, z_1, \omega) = \frac{G^-(z_1, z_0, \omega)}{G_f^+(z_1, z_0, \omega)}$$

$$= \frac{r_1 + r_2 e^{-i\omega 2t_2}}{1 + r_0 r_1 e^{-2i\omega t_1} + r_0 r_2 e^{-2i\omega(t_1 + t_2)} + r_1 r_2 e^{-2i\omega t_2}}. \tag{16}$$

Following a similar procedure in the deconvolution imaging section, the time-domain expansion of equation 16 is

$$\widetilde{R_0}(z_1, z_1 t) = r_1 \delta(t) + E(t > 0). \tag{17}$$

Consequently, the deconvolution image, $\widetilde{R_0}$ at zero time at z_1 is r_1, the true reflectivity at this location, as shown in Table 1. Thus, although we are not solving for the true reflection response R_0, our deconvolution image, using $G_f^+(z_1, t)$ and $G^-(z_1, t)$, at **time = 0** s is correct.

Because $G_f^+(z_1, t)$ excludes the multiples in G^+, we are producing the image at zero time with only the first-order Born terms. We already know that all the multiples are subtracted in the inversion to obtain the image (Snieder, 1990a, 1990b); therefore, it should come as no surprise that we produce similar images when using $G_f^+(z_1, t)$ and $G^-(z_1, t)$ or the complete $G^+(z_1, t)$ and $G^-(z_1, t)$.

Numerical investigation

Our imaging fields for the model in Figure 2 are the first arrivals of the retrieved downgoing Green's functions G_f^+ and the upgoing Green's functions G^-. A smooth version of the velocity model can be used, to compute the first arrivals and mute other events in G^+ to get G_f^+.

We follow the correlation and deconvolution imaging procedures for imaging with G_f^+ and G^-. Figures 9 and 10 show the corresponding correlation image and the deconvolution image, respectively.

Note that the correlation image (Figure 9) has no false interfaces approximately 0.7 km compared with Figure 5 because G_f^+ does not include any multiples, only the first arrival of G^+. The free-surface
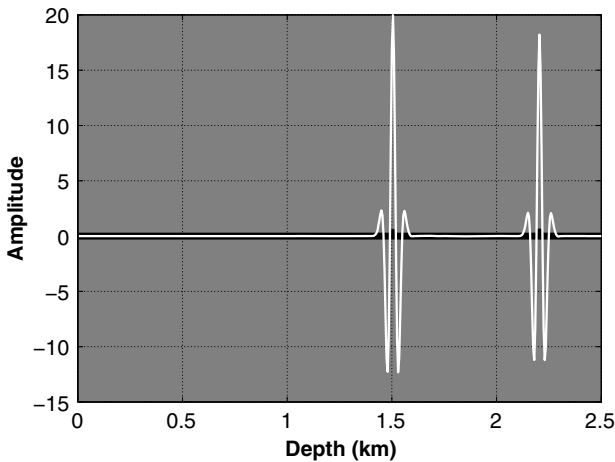

Figure 9. Correlation imaging of the first arrival of the downgoing Green's function with the upgoing Green's function for the model in Figure 2.
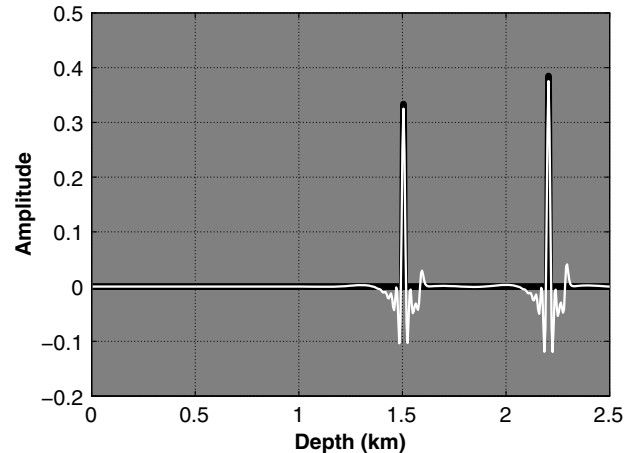

Figure 10. Deconvolution imaging of the first arrival of the downgoing Green's function with the upgoing Green's function for the model in Figure 2. The black line represents the exact reflection coefficient of the model in Figure 2.

multiple "A" in Figure 3e, no longer exists in G_f^+ and therefore does not contribute to a false interface. However, the amplitudes of the reflectors for the correlation image still do not match the true reflectivity, even though the image does not include false interfaces, as illustrated in Table 1.

The deconvolution image (Figure 10) matches the true reflectivity of the model (solid black line), despite approximating G^+ with G_f^+. We do not get the artifacts at 0.7 km in Figure 10 compared with Figure 6 (deconvolution image with G^+ and G^-). Therefore, imaging with G_f^+ and G^- removes the false interface at 0.7 km and gives the correct reflectivity of the subsurface. However, we are not able to reconstruct the correct redatumed response $R_0(z, z, t)$, as summarized in Table 1.

2D STRATEGIES FOR IMAGING

The equations that govern imaging of the retrieved Green's functions in multidimensions are similar to the imaging equations in 1D, except in 2D, they have an additional horizontal spatial variable. In 2D, an analytical investigation of Marchenko imaging with different imaging conditions is not feasible; thus, we restrict our analysis to a numerical investigation.

In this section, the spatial coordinates are defined by their horizontal and depth components; for instance, $\mathbf{x_0} = (\mathbf{x_{H,0}}, x_{3,0})$, where $\mathbf{x_{H,0}}$ are the horizontal coordinates at a depth $x_{3,0}$. Similar to the 1D section, superscript $(+)$ refers to downgoing waves and $(-)$ to upgoing waves at the observation point $\mathbf{x}$. Note that the 2D reflection response in this paper is generated with the finite-difference package in Thorbecke and Draganov (2011).

The governing equation for imaging with up- and downgoing wavefields in 2D is

$$G^-(\mathbf{x_i'}, \mathbf{x_0''}, t) = \int_{\partial D_i} d\mathbf{x_i} \int_{-\infty}^{\infty} G^+(\mathbf{x_i}, \mathbf{x_0''}, t - t')$$
$$\times R_0(\mathbf{x_i'}, \mathbf{x_i}, t')dt', \tag{18}$$

where ∂D_i is an arbitrary depth level and R_0 is the reflection response of the medium below ∂D_i (Claerbout, 1985; Amundsen, 2001; Wapenaar et al., 2008). Unlike the 1D equation 1, there is an additional integration over space $\mathbf{x_i}$. Note that $R_0(\mathbf{x_i'}, \mathbf{x_i}, t)$ is the reflection response for sources and receivers on ∂D_i, with

the medium above ∂D_i being homogeneous. The image of the subsurface in 2D is not only the reflection response R_0 at zero time but also at zero offset $R_0(\mathbf{x_i}, \mathbf{x_i}, t = 0)$. Note that the summary in Table 1 holds for 1D and for multidimensions, so we will not repeat the imaging analysis in the previous section (where the 1D imaging section rigorously analyzed Marchenko imaging with different imaging conditions), but instead, we compare Marchenko imaging with conventional RTM.

We use the velocity and density models in Figures 11 and 12, respectively, to compute the reflection response R at the surface. The reflection response R includes primaries, internal and free-surface multiples. We use the reflection response at the surface and a smooth version of the velocity Figure 13 as inputs for all imaging examples in this section. Our goal is to image a target area in the subsurface, which is enclosed by the box in Figure 11; the magnified area of the velocity is shown in Figure 14.

We first show the image we obtain from RTM in Figure 15. We construct the RTM image by evaluating the correlation of the back-propagated reflection response and forward-propagated source function in the smooth-velocity model given in Figure 13 at zero time and zero offset. We call this the RTM correlation imaging condition (Baysal et al., 1983; Whitmore, 1983), which is different
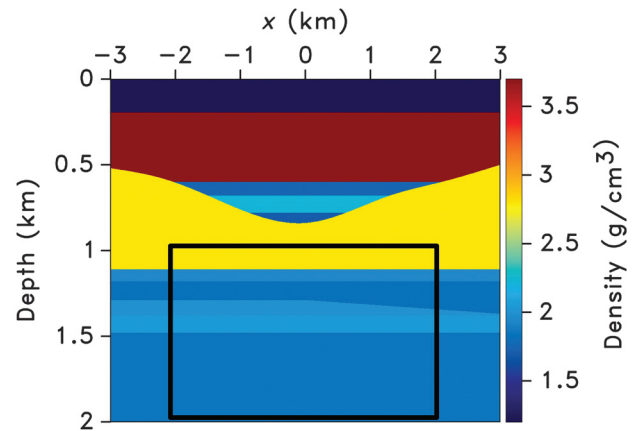

Figure 12. The density model ranging used in the 2D imaging section. The black box bounds the target area.
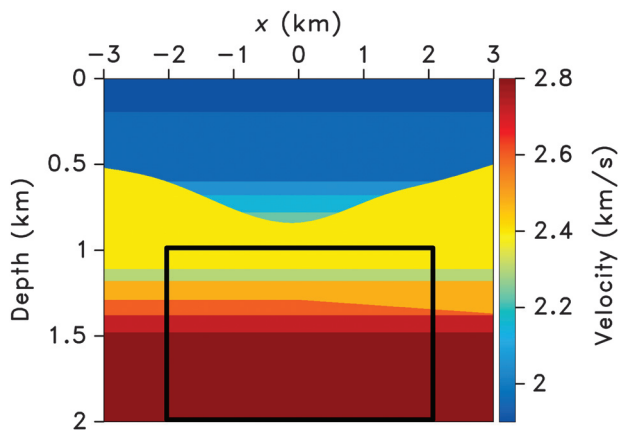

Figure 11. The velocity model used in the 2D imaging section. The black box bounds the target area.
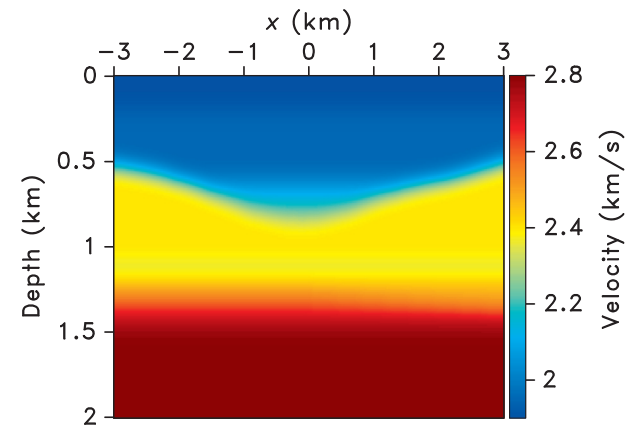

Figure 13. Macromodel, i.e., the smooth version of Figure 11, used to compute the first arrivals from the virtual source location to the surface.

from the correlation imaging condition previously mentioned that uses the up- and downgoing Green's functions. The RTM image in Figure 15 is a magnified version of the entire image at the target area. The free-surface multiples generated by the syncline above the target area as well as internal multiples contaminate the image in Figure 15 when compared with the model of the target area in Figure 14.

We now investigate Marchenko imaging of the target area in Figure 14 with the following imaging conditions: (1) correlation, (2) MDD, and (3) deconvolution. We compare the images generated by these imaging conditions constructed with either G^+ and G^- or with G_f^+ and G^-. In addition, we include a subsection that uses the redatumed reflection response to image the subsurface. Note that the associated Marchenko images are constructed from the same inputs as RTM, i.e., the reflection response at the surface and the smooth velocity model in Figure 13. We begin with the correlation imaging condition using the retrieved Green's function.

Correlation imaging in 2D

The multidimensional correlation in the frequency domain for the retrieved up- and downgoing Green's function is

$$C(\mathbf{x_i}, \mathbf{x_i'}, \omega) = \int_{\partial D_0} G^-(\mathbf{x_i}, \mathbf{x_0''}, \omega) G^+(\mathbf{x_i}, \mathbf{x_0''}, \omega)^* d\mathbf{x_0''}. \quad (19)$$

The integral of $C(\mathbf{x_i}, \mathbf{x_i}, \omega)$ over all frequencies at zero-offset is the correlation imaging condition. Conversely, in the time domain, the correlation imaging condition is the zero-offset and zero-time contribution of equation 2, $C(\mathbf{x_i}, \mathbf{x_i}, t = 0)$. The correlation images using the retrieved Green's functions are shown in Figure 16.

We construct each image point independently of the other image points and therefore we build a subset of the image; this process is called target-oriented imaging. Figure 16 is obtained by computing the Green's function $G^\pm(\mathbf{x_0''}, \mathbf{x_i'}, t)$ at the surface for virtual receivers, at intervals of 4 m, in the target area; the image is the superposition of the correlation imaging condition at each Green's function virtual receiver location. In the Marchenko image in Figure 16, the reflectors are clearly discernible and match the interfaces in the target area in Figure 14. In the imaging box, the artifacts from

the free-surface and internal multiples are no longer visible compared with the RTM image in Figure 15.

Multidimensional deconvolution imaging

As mentioned earlier, solving equation 18 for R_0 in a 1D requires deconvolution (equation 8). However, in a higher dimension, we solve equation 18 for R_0 by MDD. In the frequency domain, equation 18 becomes

$$G^-(\mathbf{x_i'}, \mathbf{x_0''}, \omega) = \int_{\partial D_i} G^+(\mathbf{x_i}, \mathbf{x_0''}, \omega) R_0(\mathbf{x_i'}, \mathbf{x_i}, \omega) d\mathbf{x_i}. \quad (20)$$

To solve equation 20 (discussed in Wapenaar et al., 2014) we first multiply both sides of the equation by G^+ and integrate over source positions at the acquisition surface x_0'' to yield

$$C(\mathbf{x_i'}, \mathbf{x_i'''}, \omega) = \int_{\partial D_i} \Gamma(\mathbf{x_i'}, \mathbf{x_i'''}, \omega) R_0(\mathbf{x_i}, \mathbf{x_i'}, \omega) d\mathbf{x_i}, \quad (21)$$

Figure 15. Magnified image of the RTM for the model in Figure 14 below the syncline structure (in the target area). The reflection response used for imaging includes primaries, internal multiples, and free-surface multiples.
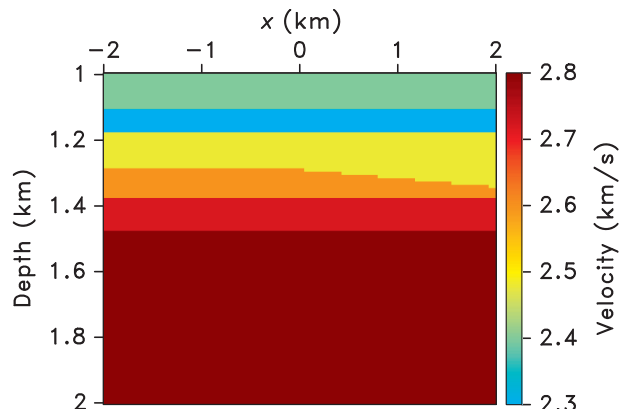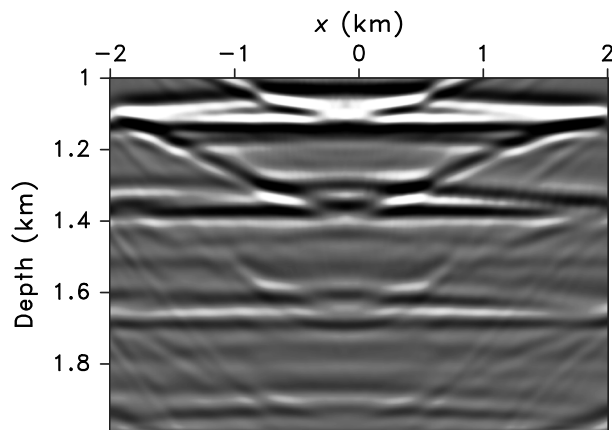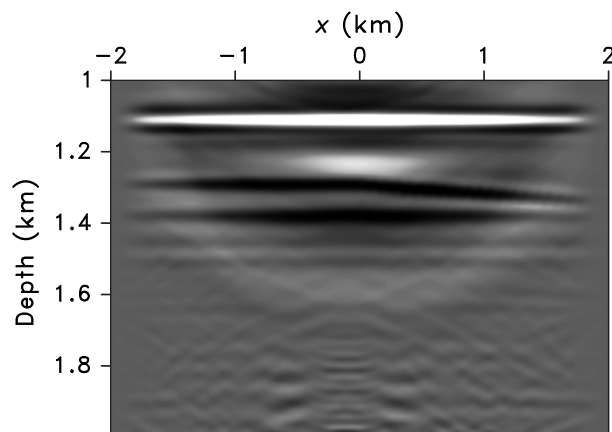

Figure 14. Target zone in the numerical model (velocity), in which we conduct imaging. Note, we do not use this model to implement Marchenko imaging, we use a smooth version of the velocity model (Figure 13) only.

Figure 16. Marchenko correlation imaging of the model in Figure 14 in the target zone.

where the correlation function C is given in equation 19 and the point-spread function is given by

$$\Gamma(\mathbf{x_i'}, \mathbf{x_i'''}, \omega) = \int_{\partial D_i} G^+(\mathbf{x_i'}, \mathbf{x_0''}, \omega) G^+(\mathbf{x_i'''}, \mathbf{x_0''}, \omega) d\mathbf{x_0''}. \tag{22}$$

We invert equation 21 for $R_0(\mathbf{x_i}, \mathbf{x_i'}, \omega)$ (Wapenaar et al., 2008; van der Neut et al., 2011). The multidimensional deconvolution imaging condition is $R_0(x_i, x_i, t = 0)$ (the reflection response R_0 at zero offset and at $t = 0$ s). To construct the image, we compute $R_0(\mathbf{x_i}, \mathbf{x_i}, t = 0)$ at every sampled point in the image.

The Marchenko images constructed with correlation and MDD yield similar results; however, as a more instructive approach to compare these images, we show a trace at $x_1 = (-0.2)$ km less than 1 km for each of the corresponding images (see Figure 17). The traces in Figure 17 show that (1) MDD matches the true reflectivity better than the other imaging conditions and (2) the events in the traces (MDD and correlation) correspond to the interfaces in the actual model at the right locations.

The true reflectivity trace in Figure 17 is constructed by computing the reflection coefficients at zero offset at $x_1 = (-0.2)$ km less than 1 km, then convolving this trace with the Ricker wavelet used in finite-difference modeling of the reflection response at the surface.

Deconvolution imaging 2D

The MDD requires the Green's functions along the horizontal datum ∂D_i to construct an image at a point $\mathbf{x_i}$ on ∂D_i. Strictly speaking, this MDD image is not imaging at a particular target because we require the Green's functions along the datum ∂D_i. Target-oriented imaging is the image at a point using only the Green's function at that point. Similar to correlation imaging, deconvolution imaging requires only the Green's function at the virtual receiver location to construct the image at that location, hence, this is target-oriented imaging.

Deconvolution imaging in 2D is the trace-by-trace deconvolution of the up- and downgoing Green's functions at each virtual receiver location at zero offset and zero time $R_0(\mathbf{x}, \mathbf{x}, t = 0)$. Alternative techniques on the implementation of the deconvolution imaging

condition are given by Schleicher et al. (2007). The deconvolution image yields similar results to correlation; therefore, we show a trace of the deconvolution image for a closer analysis (see Figure 17). The trace of the deconvolution image in Figure 17 places the reflector at the correct location, but it does not match the true reflectivity of the model, as is also summarized in Table 1. The traces of the correlation and deconvolution are scaled to match the reflectivity of the interface at 1.1 km because neither correlation nor deconvolution give the true reflection coefficients; however, in 1D, deconvolution imaging does match the true reflectivity as explained in the 1D imaging section.

Imaging with the redatumed reflection response in 2D

Similar to the 1D example on redatuming, we use the up- and downgoing Green's function at virtual receivers $\mathbf{x_i'} = (-2 \text{ to } 2, 1)$ km to compute the redatumed reflection response R_0 given in equation 18, and we use this response to image the subsurface using standard imaging algorithms. To retrieve the redatumed response $R_0(\mathbf{x_i}, \mathbf{x_i'}, t)$ accurately, we solve equation 21 by MDD. We perform RTM using the redatumed response $R_0(\mathbf{x_i}, \mathbf{x_i'}, t)$ at $\mathbf{x_i} = (-2 \text{ to } 2, 1)$ km to image the target area (see Figure 18). The RTM correlation imaging condition is used to construct the redatumed RTM in Figure 18 and the RTM with surface recordings in Figure 15.

In Figure 18, the artifacts are dramatically reduced compared with the RTM image in Figure 15. Specifically, the multiples from the syncline structure are not present in the image in Figure 18 using the redatumed response compared with the RTM in Figure 15. This reduction in artifacts is a result of the fact that the redatumed reflection response R_0 only includes the reflections less than 1 km. However, the redatumed reflection response retains internal multiples from the interfaces below the redatuming depth. Therefore, the redatumed RTM image has artifacts from such internal multiples, for instance, at $z = 1.68$ km in Figure 18, but they are significantly weaker than the reflections caused by the overburden, i.e., the syncline reflections (see Figure 15). In higher dimensions, trace-by-trace deconvolution does not solve for R_0 in equation 18 (because we have the integral over space $d\mathbf{x_i'}$ on the right side,
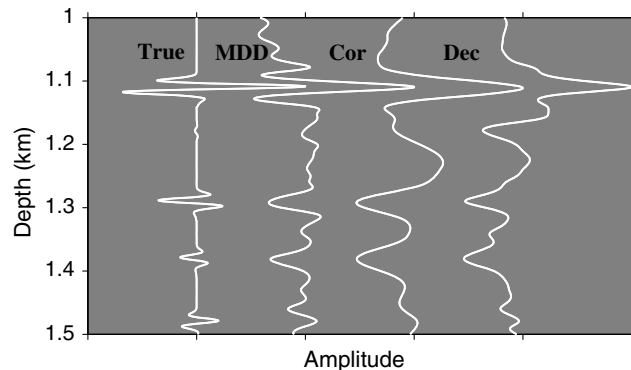

Figure 17. Comparison of the imaging conditions: MDD, correlation (Cor), and deconvolution (Dec), of the downgoing Green's function with the upgoing Green's function for the model in Figure 14 at horizontal location −0.2 km in the target area.
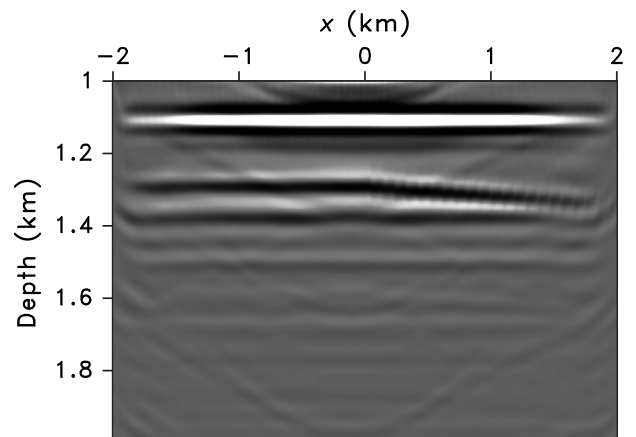

Figure 18. The RTM of the redatumed reflection response in the target area. The redatumed reflection response $R_0(\mathbf{x_i}, \mathbf{x_i'}, t)$ is the reflection response obtained by MDD of the up- and downgoing Green's function at $\mathbf{x_i} = (-2 \text{ to } 2, 1)$ km.

which we do not account for), and therefore we cannot use R_0 obtained by deconvolution to perform imaging of the subsurface by standard imaging algorithms. The images obtained from these algorithms using R_0 (by deconvolution) will include additional artifacts due to the errors in R_0.

Imaging with the first arrival of G^+ (G_f^+) and G^- in 2D

We performed correlation, deconvolution, and MDD imaging condition using G_f^+ and G^-; those are the same as the images constructed with G^+ and G^- using the same imaging conditions for our 2D examples. Figure 19 shows a comparison among the true reflectivity, a trace from the MDD imaging with G^+ and G^-, and MDD imaging with G_f^+ and G^-. As expected from the 1D imaging section, imaging with G^+ and G^- or imaging with G_f^+ and G^- gives similar contributions at the interfaces.

However, similar to the 1D imaging section, using G_f^+ and G^- does not give the correct redatumed response, and hence it should not be used to create an image below the redatuming depth.

DISCUSSION

The findings of this paper are summarized in Table 1. Starting with the first imaging condition in Table 1, correlation imaging with
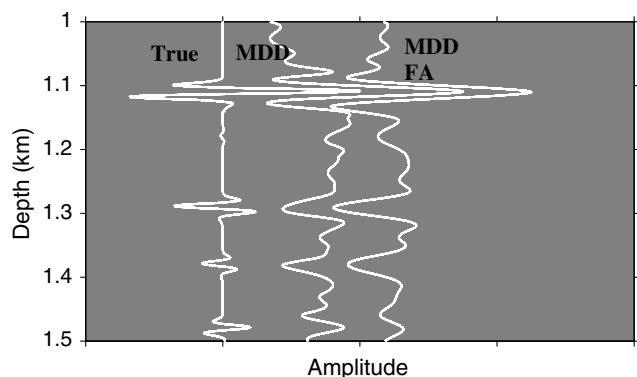

Figure 19. The MDD imaging of first arrival of downgoing Green's function with upgoing Green's function (MDD FA) for the model in Figure 14 at horizontal location −0.2 km in the target area compared with the true reflectivity and MDD imaging with the complete one-way Green's functions.
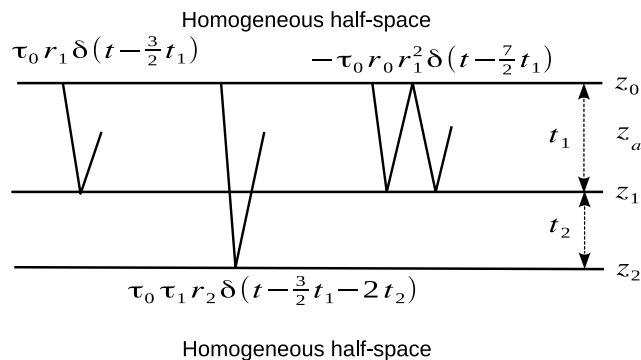

Figure 20. Ray diagram of the waves in $G^-(z_a, z_0, t)$ (equation A-10).

the retrieved Green's function gives false interfaces caused by the interaction of the reflections in G^+ and in G^-. A false interface in Marchenko correlation imaging is due to events in G^+, which exist at the same time as events in G^-. At the interface, however, all the waves in G^+ arrive at the same time as all the waves in G^-. Therefore, at the interface, the stacking of all the kinematically similar events is generally larger than at a false interface.

The MDD imaging condition applied to G^+ and G^- yields a good match with the true reflectivity and minimizes false interfaces as MDD is the theoretically accurate way to solve for the image compared with the other methods in this paper. Note that, in the imaging step, for instance equation 11, the denominators of G^+ and G^- (the multiple reflections in G^+ and G^-) cancel out. Therefore, G^+ and G^- must either have all the multiples included or G^+ and G^- must be truncated in such a way that they (G^+ and G^-) include the same order of multiples to have the multiples removed in the imaging step. Failure to include the same order of multiples in G^+ and G^- creates false interfaces in the imaging step. However, in practice, it is not feasible to know if we have the same order of multiples in G^+ and G^-. For this reason, it is more advantageous to use the first arrival of G_f^+ and G^- because we do not need to match the order of multiples in the up- and downgoing fields while still matching the true reflectivity and avoiding false interfaces.

Note that all imaging conditions using G_f^+ and G^- result in comparable or better images than using G^+ and G^-. The most advantageous use of G_f^+ and G^- is in the correlation imaging condition, in which the false interfaces are completely removed.

Even though MDD with G^+ and G^- does give the correct redatumed response with accurate reflection amplitudes, applying standard imaging to the corresponding redatumed response does not necessarily mean that the resulting image will be free of false interfaces. These false interfaces are caused by the internal-multiple reflections below the datum. However, the images constructed by the redatumed response are void of overburden reflections.

CONCLUSION

Importantly, the inputs for Marchenko imaging are exactly the same as most standard imaging techniques; a smooth version of the velocity and the reflection response at the surface. Unlike standard imaging techniques, in Marchenko imaging, we do not need to remove the free-surface or internal multiples from the reflection response because the Marchenko equations in this paper properly handle these multiples.

Although Marchenko imaging reduces the artifacts caused by multiples compared with standard imaging algorithms, these artifacts are still present. Theoretically, the correct procedure to image with the retrieved Green's functions is MDD, and therefore it best matches the correct image of the subsurface compared with other Marchenko imaging conditions. However, instead of using G^+ and G^-, Marchenko imaging with the first arrival of the downgoing Green's function G_f^+ and the associated upgoing Green's function G^-, removes these artifacts corresponding to false interfaces. Despite the fact that G_f^+ does not contain the reflection events, the resulting MDD image better matches the true reflectivity of the model compared with standard imaging or Marchenko imaging with correlation or deconvolution. Note that because only the primaries contribute to the construction of the image, whereas the multiples are implicitly removed in the inversion process to produce the

image, it suffices to only use G_f^+ and G^- compared with G^+ and G^- in the imaging.

APPENDIX A

RETRIEVING THE GREEN'S FUNCTIONS ANALYTICALLY USING THE MARCHENKO EQUATIONS

For a three-interface model (two layers) in Figure 1,

1) The first interface is just below the acquisition surface with reflection and transmission coefficients r_0 and τ_0.
2) Similarly, r_1, τ_1, r_2, and τ_2 are the reflection and transmission coefficients of the second and third interfaces, respectively.
3) The one-way traveltime in the first layer (between the first and second interfaces) is t_1.
4) The one-way traveltime in the second layer is t_2.

The reflection response for the three-interface model (two layers) for sources and receivers on the surface in Figure 1, in the frequency domain, is (Goupillaud, 1961)

$$R(z_0, \omega) = \frac{r_0 + r_1 e^{-2i\omega t_1} + r_2 e^{-2i\omega(t_1+t_2)} + r_0 r_1 r_2 e^{-2i\omega t_2}}{1 + r_0 r_1 e^{-2i\omega t_1} + r_0 r_2 e^{-2i\omega(t_1+t_2)} + r_1 r_2 e^{-2i\omega t_2}},$$

(A-1)

where r_0, r_1, and r_2 are the reflection coefficients of the layers in order of increasing depth, respectively, and t_1 and t_2 are the one-way traveltime of the first and second layers, respectively.

We use the reflection response of this three-interface model to compute the Green's functions at two locations in the model: (1) in the middle of the first layer ($z = z_a$) and (2) just above the second interface ($z = z_1$), in Figure 1.

Numerically, we retrieve these Green's function by solving the Marchenko equations (Broggini et al., 2012; Broggini and Snieder, 2012; Wapenaar et al., 2013, 2014; Slob et al., 2014; Singh et al., 2015, 2016).

Here, because the model is known, we compute the focusing functions $f_1^\pm$ (Slob et al., 2014) directly

$$f_1^+(z_i, z_0, \omega) = \frac{1}{T^+(z_i, z_0, \omega)},$$

(A-2)

$$f_1^-(z_i, z_0, \omega) = \frac{R(z_0, z_0, \omega)}{T^+(z_i, z_0, \omega)},$$

(A-3)

where z_0 and z_1 are the depths of the first and second reflector, $R(z_0, z_0, \omega)$ is the reflection response at the surface for a source at z_0, and $T^+(z_i, z_0, \omega)$ is the transmission response at z_i for a source at z_0.

The Marchenko equations relating the Green's functions $G^\pm$ to the focusing functions $f_1^\pm$ are

$$G^-(z_i, z_0, \omega) = f_1^+(z_0, z_i, \omega)R(z_0, z_0, \omega) - f_1^-(z_0, z_i, \omega),$$

(A-4)

and

$$G^+(z_i, z_0, \omega) = -f_1^-(z_0, z_i, \omega)^* R(z_0, z_0, \omega) + f_1^+(z_0, z_i, \omega)^*,$$

(A-5)

where $G^\pm(z_i, z_0, \omega)$ are the one-way Green's functions at z_i for a source at z_0 (Broggini et al., 2012; Broggini and Snieder, 2012; Wapenaar et al., 2013, 2014; Slob et al., 2014; Singh et al., 2015, 2016). The one-way Green's functions are decomposed at the observation point z denoted by the first superscript $+$ or $-$. We consider downward to be positive; hence, the superscript $+$ represents downgoing waves and $-$ upgoing waves.

The focusing functions are auxiliary wavefields that reside in a truncated medium that (1) has the same material properties as the actual inhomogeneous medium between z_0 and z_i (arbitrary depth level) and (2) is homogeneous above z_0 and is reflection-free below z_i (Slob et al., 2014). Therefore, the boundary conditions on z_0 and z_i in the truncated medium, in which the focusing function exists, are reflection-free.

GREEN'S FUNCTION RETRIEVAL IN THE MIDDLE OF THE FIRST LAYER z_a

The focusing function exist in a truncated medium, which we label Υ_a. At z_a, we define the truncated medium Υ_a as homogeneous at and below z_a and the same as the actual model above z_a. Therefore, for this truncated medium Υ_a, the reflection response $R(z_0, z_0, \omega)$ in the frequency domain is r_0, whereas the transmission response $T(z = z_a, z_0, \omega) = \tau_0 e^{i\omega t_1/2}$.

Substituting the reflection and the transmission response for the truncated medium Υ_a into equations A-2 and A-3 yields

$$f_1^+(z_a, z_0, \omega) = \frac{r_0}{\tau_0} e^{i\omega t_1/2},$$

(A-6)

$$f_1^-(z_a, z_0, \omega) = \frac{1}{\tau_0} e^{i\omega t_1/2}.$$

(A-7)

We retrieve the up- and downgoing Green's function $G^\pm(z_a, z_0, \omega)$ by substituting equations A-1, A-6, and A-7 into equations A-4 and A-5

$$G^-(z_a, z_0, \omega)$$
$$= \tau_0 \frac{r_1 e^{-\frac{3}{2}i\omega t_1} + r_2 e^{-i\omega\left(\frac{3}{2}t_1 + 2t_2\right)}}{1 + r_0 r_1 e^{-2i\omega t_1} + r_0 r_2 e^{-2i\omega(t_1+t_2)} + r_1 r_2 e^{-2i\omega t_2}},$$

(A-8)

$G^+(z_a, z_0, \omega)$

$$= \tau_0 \frac{e^{-\frac{1}{2}i\omega t_1} + r_1 r_2 e^{-i\omega(\frac{1}{2}t_1 + 2t_2)}}{1 + r_0 r_1 e^{-2i\omega t_1} + r_0 r_2 e^{-2i\omega(t_1 + t_2)} + r_1 r_2 e^{-2i\omega t_2}}.$$

$$(A\text{-}9)$$

To verify our result, we compute the time-domain expression for the series expansion of equation A-8 to yield

$$
\begin{aligned}
G^-(z_a, z_0, t) = \tau_0 \bigg\{ & r_1 \delta\left(t - \frac{3}{2}t_1\right) + r_2 \delta\left(t - \frac{3}{2}t_1 - 2t_2\right) \\
& - r_0 r_1^2 \delta\left(t - \frac{7}{2}t_1\right) - r_1^2 r_2 \delta\left(t - \frac{3}{2}t_1 - 2t_2\right) + \cdots \bigg\}, \\
= \tau_0 \bigg\{ & r_1 \delta\left(t - \frac{3}{2}t_1\right) + \tau_1^2 r_2 \delta\left(t - \frac{3}{2}t_1 - 2t_2\right) \\
& - r_0 r_1^2 \delta\left(t - \frac{7}{2}t_1\right) + \cdots \bigg\},
\end{aligned}
$$

$$(A\text{-}10)$$

where $\tau_1^2 = 1 - r_1^2$ and t_1 and t_2 describe the time for a wave to traverse, in one direction, the length of the first and second layers, respectively. These waves in equation A-10 are shown in the ray diagram (see Figure 20), and they correctly correspond to the events in Figure 1. Note that the retrieval of the Green's function in equation A-10 takes into account the transmission coefficients of the layers.

GREEN'S FUNCTION RETRIEVAL AT THE SECOND LAYER z_1

To retrieve the Green's function at the second layer $z = z_1$, we analytically compute the reflection response at z_0 and the transmission response at z_1 for the truncated medium Υ_1. The truncated medium Υ_1 is homogeneous at and below z_1 and the same as the actual model above z_1. For this reason, the reflection response for the truncated medium Υ_1 remains the same as the reflection response in the truncated medium Υ_a because no new interfaces are included.

The transmission response for the truncated medium Υ_1 becomes $T(z = z_1, z_0, \omega) = \tau_0 e^{i\omega t_1}$. The corresponding focusing functions become

$$f_1^+(z_1, z_0, \omega) = \frac{r_0}{\tau_0} e^{i\omega t_1}, \qquad (A\text{-}11)$$

$$f_1^-(z_1, z_0, \omega) = \frac{1}{\tau_0} e^{i\omega t_1}. \qquad (A\text{-}12)$$

Substituting equations A-1, A-11, and A-12 into equations A-4 and A-5 yields the Green's function at the second layer:

$G^-(z_1, z_0, \omega)$

$$= \tau_0 \frac{r_1 e^{-i\omega t_1} + r_2 e^{-i\omega(t_1 + 2t_2)}}{1 + r_0 r_1 e^{-2i\omega t_1} + r_0 r_2 e^{-2i\omega(t_1 + t_2)} + r_1 r_2 e^{-2i\omega t_2}},$$

$$(A\text{-}13)$$

$G^+(z_1, z_0, \omega)$

$$= \tau_0 \frac{e^{-i\omega t_1} + r_1 r_2 e^{-i\omega(t_1 + 2t_2)}}{1 + r_0 r_1 e^{-2i\omega t_1} + r_0 r_2 e^{-2i\omega(t_1 + t_2)} + r_1 r_2 e^{-2i\omega t_2}}.$$

$$(A\text{-}14)$$

REFERENCES

Amundsen, L., 2001, Elimination of free-surface related multiples without need of the source wavelet: Geophysics, **66**, 327–341, doi: 10.1190/1.1444912.

Bakulin, A., and R. Calvert, 2006, The virtual source method: Theory and case study: Geophysics, **71**, no. 4, SI139–SI150, doi: 10.1190/1.2216190.

Baysal, E., D. D. Kosloff, and J. W. Sherwood, 1983, Reverse time migration: Geophysics, **48**, 1514–1524, doi: 10.1190/1.1441434.

Behura, J., K. Wapenaar, and R. Snieder, 2012, Newton-Marchenko-Rose imaging: 82nd Annual International Meeting, SEG, Expanded Abstracts, doi: 10.1190/segam2012-1531.1.

Broggini, F., and R. Snieder, 2012, Connection of scattering principles: A visual and mathematical tour: European Journal of Physics, **33**, 593–613, doi: 10.1088/0143-0807/33/3/593.

Broggini, F., R. Snieder, and K. Wapenaar, 2011, Connection of scattering principles: Focusing the wavefield without source or receiver: 81st Annual International Meeting, SEG, Expanded Abstracts, 3845–3850.

Broggini, F., R. Snieder, and K. Wapenaar, 2012, Focusing the wavefield inside an unknown 1D medium: Beyond seismic interferometry: Geophysics, **77**, no. 5, A25–A28, doi: 10.1190/geo2012-0060.1.

Broggini, F., R. Snieder, and K. Wapenaar, 2014, Data-driven wavefield focusing and imaging with multidimensional deconvolution: Numerical examples for reflection data with internal multiples: Geophysics, **79**, no. 3, WA107–WA115, doi: 10.1190/geo2013-0307.1.

Claerbout, J., 1985, Imaging the earth's interior: Blackwell Scientific Publications.

Clayton, R., and R. Wiggins, 1976, Source shape estimation and deconvolution of teleseismic body waves: Geophysical Journal of the Royal Astronomical Society, **47**, 151–177, doi: 10.1111/j.1365-246X.1976.tb01267.x.

Glogovsky, V., E. Landa, and J. Paffenholz, 2002, Integrated approach to subsalt depth imaging: Synthetic case study: The Leading Edge, **21**, 1217–1223, doi: 10.1190/1.1536137..

Goupillaud, P. L., 1961, An approach to inverse filtering of near-surface layer effects from seismic records: Geophysics, **26**, 754–760, doi: 10.1190/1.1438951.

McMechan, G. A., 1989, A review of seismic acoustic imaging by reverse-time migration: International Journal of Imaging Systems and Technology, **1**, 18–21, doi: 10.1002/(ISSN)1098-1098.

Mehta, K., A. Bakulin, J. Sheiman, R. Calvert, and R. Snieder, 2007, Improving the virtual source method by wavefield separation: Geophysics, **72**, no. 4, V79–V86, doi: 10.1190/1.2733020.

O'Brien, M. J., and S. H. Gray, 1996, Can we image beneath salt?: The Leading Edge, **15**, 17–22, doi: 10.1190/1.1437194.

Schleicher, J., J. Costa, and A. Novais, 2007, A comparison of imaging conditions for wave equation shot-profile migration: Geophysics, **73**, no. 6, S219–S227, doi: 10.1190/1.2976776.

Singh, S., R. Snieder, J. Behura, J. van der Neut, K. Wapenaar, and E. Slob, 2015, Marchenko imaging: Imaging with primaries, internal multiples, and free-surface multiples: Geophysics, **80**, no. 5, S165–S174, doi: 10.1190/geo2014-0494.1.

Singh, S., R. Snieder, J. Thorbecke, J. van der Neut, K. Wapenaar, and E. Slob, 2016, Accounting for free surface multiples in Marchenko imaging: Geophysics, **82**, no. 1, R19–R30, doi: 10.1190/geo2015-0646.1.

Slob, E., K. Wapenaar, F. Broggini, and R. Snieder, 2014, Seismic reflector imaging using internal multiples with Marchenko-type equations: Geophysics, **79**, no. 2, S63–S76, doi: 10.1190/geo2013-0095.1.

Snieder, R., 1990a, A perturbative analysis of nonlinear inversion: Geophysical Journal of International, **101**, 545–556, doi: 10.1111/j.1365-246X.1990.tb05569.x.

Snieder, R., 1990b, The role of the Born-approximation in nonlinear inversion: Inverse Problems, **6**, 247–266, doi: 10.1088/0266-5611/6/2/008.

Thorbecke, J. W., and D. Draganov, 2011, Finite-difference modeling experiments for seismic interferometry: Geophysics, **76**, no. 6, H1–H18, doi: 10.1190/geo2010-0039.1.

van der Neut, J., J. Thorbecke, K. Mehta, E. Slob, and K. Wapenaar, 2011, Controlled source interferometric redatuming by cross correlation and multidimensional deconvolution in elastic media: Geophysics, **76**, no. 4, SA63–SA76, doi: 10.1190/1.3580633.

Wapenaar, K., F. Broggini, E. Slob, and R. Snieder, 2013, Three-dimensional single-sided Marchenko inverse scattering, data-driven focusing, Green's function retrieval, and their mutual relations: Physical Review Letters, **110**, 084301, doi: 10.1103/PhysRevLett.110.084301.

Wapenaar, K., F. Broggini, and R. Snieder, 2011, A proposal for model-independent 3D wave field reconstruction from reflection data: 81st Annual International Meeting, SEG, Expanded Abstracts, 3788–3792.

Wapenaar, K., F. Broggini, and R. Snieder, 2012, Creating a virtual source inside a medium from reflection data: Heuristic derivation and stationary-phase analysis: Geophysical Journal International, **190**, 1020–1024.

Wapenaar, K., E. Slob, and R. Snieder, 2008, Seismic and electromagnetic controlled-source interferometry in dissipative media: Geophysical Prospecting, **56**, 419–434, doi: 10.1111/j.1365-2478.2007.00686.x.

Wapenaar, K., J. Thorbecke, J. van der Neut, F. Broggini, E. Slob, and R. Snieder, 2014, Marchenko imaging: Geophysics, **79**, no. 3, WA39–WA57, doi: 10.1190/geo2013-0302.1.

Weglein, A., and W. Dragoset, 2007, Multiple attenuation: SEG.

Whitmore, N. D., 1983, Iterative depth migration by backward time propagation: 53rd Annual International Meeting, SEG, Expanded Abstracts, 382–385.